Materials Advances

ROYAL SOCIETY OF CHEMISTRY

PAPER

View Article Online
View Journal | View Issue

Cite this: *Mater. Adv.*, 2025, 6, 9113

Hydrophobic and hydrophilic carbon supports for iron-based CO_2 hydrogenation catalysts: impact on high-pressure low-temperature reverse water gas shift and Fischer–Tropsch synthesis

Weixin Meng,[a] Sri Rezeki,[b] A. Iulian Dugulan,[c] Martin Oschatz [bd] and Jingxiu Xie *[a]

CO_2 hydrogenation into long-chain hydrocarbons offers a potential contribution towards achieving a sustainable carbon cycle. The reverse water gas shift (RWGS) process converts CO_2 and H_2 to CO and H_2O, enabling the use of CO as a carbon feedstock by utilizing existing syngas (CO and H_2) conversion technologies. Most RWGS processes operate at high temperatures (>600 °C) and ambient pressure due to favorable thermodynamics, whereas lower temperatures and higher pressures are preferred for subsequent syngas conversion *via* Fischer–Tropsch synthesis (FTS). H_2O is an inherent by-product of both processes with highly oxidizing properties and may influence the catalytic performance. This study investigates the effects of hydrophobic and hydrophilic carbon-supported Fe-based catalysts on RWGS and FTS. HNO_3 reflux treatment of the pristine hydrophobic carbon support is performed to introduce hydrophilicity. The overall hydrophilicity of the catalysts depends on both the carbon support and the Fe loading, as Fe-based nanoparticles also exhibit hydrophilic characteristics. H_2O vapor sorption and contact angle measurements are employed to assess the catalysts' H_2O affinity, which is linked to the catalytic properties, giving consistent results. Catalytic performance is evaluated at 300 °C, 11 bar, $H_2/CO_2/Ar$ = 3/1/1, 600–500 000 mL g_{cat}^{-1} h^{-1}. RWGS is investigated at CO_2 conversions below the equilibrium limit of 23%, and the more hydrophobic catalyst exhibits higher activity and CO selectivity compared to the more hydrophilic catalysts. Notably, the Sabatier reaction emerges as a competing pathway for 5 wt% Fe-based catalysts supported on more hydrophilic carbon. This higher CO_2 methanation is likely facilitated by hydrogen transfer from the carbon support, and it can be suppressed by larger Fe nanoparticle size and higher Fe loading. No significant influence of support hydrophilicity on either the RWGS or FTS reactions is observed for 20 wt% Fe/C catalysts, likely due to their overall hydrophilic nature resulting from the high Fe loading.

Received 21st July 2025,
Accepted 19th October 2025

DOI: 10.1039/d5ma00785b

rsc.li/materials-advances

1. Introduction

CO_2 hydrogenation presents a promising approach for converting CO_2 into chemicals and fuels, and proceeds indirectly through a CO-mediated pathway (CO_2-FTS).[1,2] CO is first produced from CO_2 *via* the reverse water gas shift (RWGS) and subsequently converted to C_{2+} hydrocarbons *via* Fischer–Tropsch synthesis (FTS).[3,4] Thermodynamically, RWGS is an endothermic reaction favored at high temperatures (>500 °C) and ambient pressures, whereas the subsequent FTS is an exothermic reaction preferred at lower temperatures (200–350 °C) and higher pressures.[5–8] These typical FTS conditions are also favorable for the Sabatier reaction, leading to the formation of the undesired methane.[9] Fe-based catalysts are widely applied in CO_2-FTS due to their ability to activate CO_2, H_2, as well as CO, and to enable C–C coupling simultaneously.[10,11] Fe_3O_4 and Fe_5C_2 are generally considered to be the most active phases for RWGS and FTS, respectively.[12]

H_2O is inherently a product of CO_2 hydrogenation and influences thermodynamics, kinetics, and catalyst structural properties. Brübach *et al.* proposed that H_2O partial pressure limits CO_2 equilibrium conversion at high residence times, based on their kinetic model of the Fe/K@γ-Al_2O_3 catalyst at 300 °C, 10 bar, H_2/CO_2 = 3.[13] Furthermore, H_2O and its derivatives (H*, OH*, and O*) are proposed to play a vital role in the

[a] *Green Chemical Reaction Engineering, Engineering and Technology Institute Groningen, University of Groningen, Nijenborgh 3, 9747 AG Groningen, The Netherlands. E-mail: jingxiu.xie@rug.nl*
[b] *Friedrich-Schiller-University Jena, Institute for Technical Chemistry and Environmental Chemistry, Philosophenweg 7a, 07743 Jena, Germany*
[c] *Laboratory of Fundamentals Aspects of Materials and Energy, Department of Radiation Science & Technology, Delft University of Technology, Mekelweg 15, 2628 CD Delft, the Netherlands*
[d] *Friedrich-Schiller-University Jena, Chemistry, Center for Energy and Environmental Chemistry Jena (CEEC Jena), Philosophenweg 7a, 07743 Jena, Germany*

reaction mechanism of CO_2-FTS. Adsorbed H_2O and its derivatives on the catalyst surface may occupy the active sites for CO_2/CO/H_2 dissociation and inhibit the reaction.[14,15] Alternatively, H_2O and its derivatives may interact with the reactants to alter the reaction pathway and increase the reaction rate.[16,17] H_2O and its derivatives acting as the hydrogen source or H-shuttling mediator are reviewed to improve CO activation and dissociation, further enhancing the surface coverage of polymerization intermediates and promoting the formation of long-chain hydrocarbons.[15] From the perspective of catalyst structural properties, H_2O may accelerate sintering and oxidation of iron carbide to iron oxide, and the loss of active sites and phase transformation decrease catalytic activity and selectivity towards long-chain hydrocarbons.[18,19] The degree of catalyst deactivation depends on the H_2O partial pressures in the reactor, which increases with increasing residence time and CO_2 conversion.[20]

The hydrophobicity or hydrophilicity of catalysts has a significant effect on H_2O adsorption, desorption, and diffusion.[21] A common strategy to attain surface hydrophobicity in bulk catalysts is to construct a hydrophobic shell that encapsulates the catalyst.[22,23] However, the core–shell structure may cover the active sites, resulting in a loss of catalyst activity.[24] On the other hand, hydrophobicity may be introduced to supported catalysts *via* support modification.[25–28] Support modification after incorporation of active element nanoparticles on the supported catalyst may block pores and reduce the accessibility of reactants to active sites.[29] Therefore, support modification before incorporation of active element nanoparticles on the supported catalyst is a more promising approach to prevent the poisoning of the active sites and maintain the reducibility of the catalyst. Among typical supports for CO_2 hydrogenation, carbon is a promising material due to its high surface area, tunable surface chemistry, and weak metal-support interaction.[30] Functionalizing carbon supports with oxygen- and nitrogen-containing species is usually employed to modulate the metal support interaction, introduce anchoring sites, and stabilize metal nanoparticles.[31–37] Furthermore, such treatments do usually also alter the surface properties of the carbon support, converting its inherent hydrophobicity to hydrophilicity.[38]

The objective of this study is to investigate the effect of hydrophobic and hydrophilic carbon-supported Fe-based catalysts on the performance of RWGS and FTS for CO_2-FTS. A reflux treatment of pristine hydrophobic carbon using HNO_3 resulted in hydrophilic carbon with surface functional groups. The overall hydrophobicity or hydrophilicity of the catalysts was influenced by both the nature of the support and the Fe loading. These properties were characterized using contact angle measurements and water vapor sorption analyses. The performance was evaluated at 300 °C, 11 bar, $H_2/CO_2/Ar$ = 3/1/1, 600–500 000 mL g_{cat}^{-1} h^{-1}. Mössbauer spectroscopy results revealed that the RWGS catalyst supported on more hydrophobic carbon contained more Fe oxide compared to those on hydrophilic carbon, correlating with the higher CO selectivity.

2. Experimental methods

2.1 Synthesis of carbon-supported catalysts

To prepare a hydrophilic carbon support, 7 g of pristine carbon black (Cabot, VXC 72, 75–150 μm) was treated with 140 ml 70% HNO_3 (Sigma-Aldrich) under reflux at 80 °C for 20 or 40 h. The resulting materials are named C20h and C40h, respectively. An oil bath was used to control the temperature of the suspension. The carbon support was then washed several times with deionized water until the pH value reached between 6 and 7. After washing, the carbon was dried at 110 °C overnight and subsequently crushed and sieved into 75–150 μm.

Fe nanoparticles were deposited on pristine C, C20h, or C40h support (75–150 μm) using incipient wetness impregnation. The carbon supports were first dried at 110 °C for 2 h to remove water. The aqueous Fe precursor solutions were obtained by dissolving ammonium iron citrate (Sigma-Aldrich, 16.5–18.5 wt% Fe) and potassium nitrate (Sigma-Aldrich, ≥99.0%) in deionized water. The solubility of the Fe salt precursor was 1 g ml^{-1} in deionized water. Methanol (H_2O : MeOH = 2 : 1 ml) was subsequently added to the aqueous precursor solution. The molar ratio of Fe/K was 10 for all catalysts. To obtain 5 wt% Fe-loaded catalysts, the precursor solution was diluted to fill the pore volume of the carbon support (0.7 cm^3 g^{-1}). 20 wt% Fe-loaded catalysts required successive impregnation steps. The samples were dried at 110 °C between the impregnation steps and after the final step for 1 h and 12 h, respectively. The dried samples were pyrolyzed at 500 °C (2 °C min^{-1}) for 2 h under N_2 flow. These catalysts are denoted as 5Fe/C, 5Fe/C20h, 5Fe/C40h, 20Fe/C, 20Fe/C20h. In addition, 5 wt% Fe-loaded catalysts pyrolyzed at 500 °C for 2 h and subsequently at 700 °C for 8 h, are denoted as 5Fe/C-700, 5Fe/C20h-700.

2.2 Characterization

Thermogravimetric analysis (TGA) was employed to determine the stability of carbon supports and catalysts as well as the Fe loading. The measurement was performed on a TA Instruments Discovery TGA 550 with platinum pans. The sample was heated from 40 to 800 °C (5 °C min^{-1}) under N_2 or synthetic air gas flow.

N_2 physisorption at −196 °C was used to measure the surface area and pore volume of the catalyst. The measurement was conducted on a Micromeritics ASAP 2420 analyzer. Prior to analysis, the samples were degassed under vacuum at 200 °C for 12 h. The specific surface area was calculated by the Brunauer–Emmett–Teller (BET) method. The pore volume was estimated from the single point desorption data at a relative pressure (P/P_0) of 0.98.

Water vapour sorption measurements were performed using an Autosorb IQ device from Quantachrome Instruments at 25 °C. Prior to any measurement, 50 mg of each sample powder was degassed overnight at 120 °C in a glass cell with a 9 mm diameter. The temperature was kept constant using a circulating water bath. The adsorption and desorption points were measured in the range of relative pressure (P/P_0) 0.01–0.9.

The contact angle (CA) measurements were performed with a Dataphysics OCA25 system. The samples were prepared by the glass slide method.[39] The microscope slide (75 × 25 mm) was

partly covered with double-sided adhesive tape. The catalyst was placed on the side of the tape and subsequently made to slide off naturally by tilting the microscope slide. After repeating several times, the catalyst was uniformly dispersed on the surface of the tape. To firmly attach the catalyst to the surface of the tape, more catalysts were evenly distributed on the surface and then a clean microscope slide was placed and pressed for 30 s. This process was repeated at least twice. A 8 μl-droplet of water was placed on the sample, and a camera recorded it over several seconds. Each measurement was repeated twice, and the error margin of the contact angle was between 5 and 10°.

Transmission electron microscopy (TEM) images were attained on a Philips CM120 (120 kV) microscope. The iron oxide averaged particle sizes were determined by individual measurements of at least 200 Fe nanoparticles. Before the measurements, the catalyst was ultrasonically dispersed in ethanol for 5 min, then dispersed on a carbon-coated Cu grid and dried for a few minutes.

In situ transmission Fe Mössbauer spectroscopy was applied to identify the evolution of Fe phases. Transmission ^{57}Fe Mössbauer spectra were collected at 4.2 K with a conventional constant-acceleration spectrometer using a ^{57}Co(Rh) source. For the 120 K measurements, a sinusoidal velocity spectrometer was used, in which the source and the absorbing samples were kept at the same temperature. Velocity calibration was carried out using an α-Fe foil at room temperature. The Mössbauer spectra were fitted using the Mosswinn 4.0 program. The experiments were performed in a state-of-the-art high-pressure Mössbauer *in situ* cell developed at Reactor Institute Delft. The high-pressure beryllium windows used in this cell contain 0.08% Fe impurity whose spectral contribution was fitted and removed from the final spectra.

2.3 Catalytic performance testing

The catalytic experiments were conducted in a fixed-bed reactor unit (Microactivity Effi, PID Eng). The catalysts (75–150 μm) were diluted with SiC (25–75 μm). The catalyst was first reduced at 400 °C (5 °C min^{-1}), 2 bar, H_2/Ar = 1/1 for 2 h. The synthesis gas mixture (H_2/CO/Ar = 2/2/1) was introduced at 280 °C, 2 bar for 20 h to carburize the catalysts. After pretreatment, the catalytic performance was tested at 300 °C, 11 bar, H_2/CO_2/Ar = 3/1/1, 600–500 000 mL g_{cat}^{-1} h^{-1}. The product stream was analyzed using online GC. The permanent gases (H_2, Ar, CO_2, CO) were separated over a Hayesep Q 60–80 column and a ShinCarbon-ST column using a thermal conductivity detector (TCD). Hydrocarbons (C_1–C_9) were separated over a GS-Gaspro column using a flame ionization detector (FID).

CO_2 conversion was calculated according to eqn (1). The product selectivity of CO and hydrocarbons up to C_9 were determined with online GC and were calculated according to eqn (2). The carbon balance was between 88–105% (eqn (S1)). Iron time yield (FTY) of CO_2 and product were expressed as moles of CO_2 converted and product formed per gram of Fe per second and were calculated according to eqn (3) and (4), respectively.

$$X_{CO_2} = \frac{CO_{2,\,in} - \frac{Ar_{in}}{Ar_{out}} \times CO_{2,\,out}}{CO_{2,\,in}} \times 100\% \quad (1)$$

$$S_{product} = \frac{\frac{Ar_{in}}{Ar_{out}} \times product_{out} \times n}{CO_{2,\,in} - \frac{Ar_{in}}{Ar_{out}} \times CO_{2,\,out}} \times 100\% \quad (2)$$

$$FTY_{CO_2} = \frac{GHSV \times m_{CO_2,\,in} \times X_{CO_2}}{W_{Fe} \times V_m} \quad (3)$$

$$FTY_{product} = \frac{GHSV \times m_{CO_2,\,in} \times X_{CO_2} \times S_{product}}{W_{Fe} \times V_m} \quad (4)$$

where GHSV represents gas hourly space velocity; $m_{CO_2,in}$ represents the molar fraction of CO_2 in the inlet gas; W_{Fe} represents the mass percentage of Fe in the catalyst; V_m represents molar volume at the standard temperature and pressure.

3. Results and discussion

3.1 Structural properties of the catalysts

The thermal stability of pristine carbon and oxidized carbons was evaluated by TGA under N_2 flow. As depicted in Fig. 1(a), the pristine carbon exhibits less than 1% weight loss between 40 to 800 °C, indicating high thermal stability under non-oxidizing conditions. For C20h and C40h, the total weight loss is approximately 10%, indicating that some functional groups

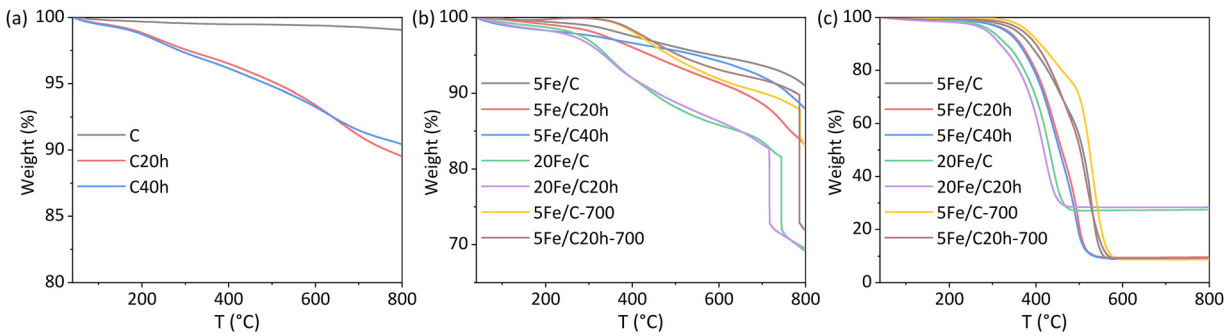

Fig. 1 TGA of (a) carbon supports, (b) fresh catalysts under N_2 flow; and (c) fresh catalysts under synthetic air flow.

have been introduced into the pristine carbon and subsequently decomposed upon heating. According to the literature, approximately 5% weight loss between 40 and 500 °C can be attributed to water vaporization and the decomposition of carboxyl, partial lactone, and anhydride groups. A further 3% weight loss between 500 and 700 °C might be caused by the decomposition of partial lactone and phenol groups. Finally, the remaining 2% weight loss from 700 to 800 °C could correspond to the decomposition of ether and carbonyl groups.[40,41] Fig. 1(b) presents the TGA curves under N_2 flow of fresh catalysts after pyrolysis at either 500 or 700 °C. For all catalysts, a slight weight loss gets evident before reaching the respective pyrolysis temperatures. The weight loss is more pronounced for the catalysts with higher Fe content and could thus be attributed to the incomplete pyrolysis of the Fe precursor or to higher water content in the most Fe-rich catalysts (as discussed below). The latter could be due to either water binding on the Fe oxide surface but also due to the higher density of functional groups on the carbon surface after decomposing a larger content of the Fe precursor. The Fe loading of fresh catalysts was estimated based on TGA data obtained under synthetic air flow. Fig. 1(c) shows that the catalysts with the theoretical Fe loadings of 5 and 20 wt% have residual weights of 9 and 28 wt%, respectively. Assuming that the residual fresh catalysts are composed primarily of Fe_2O_3 and K_2O and considering that the theoretical molar ratio of Fe to K is 10 : 1, the calculated Fe loading for the fresh catalysts is presented in Table 1, which is in good agreement with theoretical values. From Fig. 1(c), the combustion of the catalysts with 20 wt% loading occurs at a lower temperature compared to the 5 wt% loading under the synthetic air flow, and this is attributed to the higher Fe loading as Fe_2O_3 is known to catalyze the combustion of carbon.[42]

Table 1 further presents textural properties of carbon supports and fresh catalysts. The surface area of carbon support gets reduced from 212 to 154 $m^2\ g^{-1}$, and the pore volume slightly decreases from 0.7 to 0.5 $cm^3\ g^{-1}$ after 20 hours of acid treatment. No significant changes are observed upon increasing the acid treatment duration from 20 to 40 hours. The decreases in surface area and pore volume can be attributed to the destruction of pore structure and removal of amorphous carbon by the strong oxidant.[34,43] Fe impregnation leads to coverage of the carbon surface, leading to a reduction in surface area. This reduction becomes more pronounced with a higher Fe loading. 5Fe/C20h and 5Fe/C40h catalysts have rather similar textural properties due to similar C20h and C40h supports. There is no noticeable difference between 20Fe/C and 20Fe/C20h catalysts, which could be attributed to the maximum Fe loading on carbon supports. As shown in Fig. S1, the N_2 adsorption–desorption isotherms of carbon supports and fresh catalysts are relatively similar in shape, indicating no major changes in pore size distributions. They are all typical type IV isotherms with an H_3-type hysteresis loop, representing the presence of mesopores.

Table 1 Properties of carbon supports and fresh catalysts

Catalysts	Fe loading[a] (wt%)	S_{BET}[b] ($m^2\ g^{-1}$)	V_{SPD}[b] ($cm^3\ g^{-1}$)
C	—	212	0.7
C20h	—	154	0.5
C40h	—	142	0.4
5Fe/C	6	196	0.5
5Fe/C20h	6	139	0.4
5Fe/C40h	6	136	0.4
20Fe/C	18	103	0.5
20Fe/C20h	19	101	0.5
5Fe/C-700	6	171	0.6
5Fe/C20h-700	6	136	0.4

[a] Measured by TGA. [b] Measured with N_2-adsorption, S_{BET}: specific surface area by BET method, V_{SPD}: single point desorption total pore volume.

In addition to N_2 sorption measurements, H_2O vapor sorption measurements were also performed. Fig. 2 shows the isotherms of carbon supports and fresh catalysts. In general, the unoxidized pristine carbon material and corresponding catalysts (C, 5Fe/C, and 20Fe/C) show lower water uptake over the entire range of pressures than the oxidized carbon resulting from acid treatment (C20h, 5Fe/C20h, and 20Fe/C20h). The isotherms of unoxidized materials are classified as type III, indicating the weak interactions between the adsorbent and adsorbate, with water vapor molecules clustering around the most suitable places on the adsorbent's surface.[44] Meanwhile, the oxidized carbon materials exhibit type II isotherms, indicating the reversible behavior of water vapor adsorption and desorption. The shape is the consequence of unimpeded monolayer–multilayer adsorption at elevated P/P_0 levels. A diminished knee signifies considerable overlap of monolayer coverage and the initiation of multilayer adsorption. Furthermore, except 20Fe/C20h catalyst, all isotherms have hysteresis type H_3, which runs into very high adsorption volumes at high P/P_0. This hysteresis also contains a steep region at P/P_0 in the range 0.4–0.5 associated with a forced closure of the loop due to the tensile strength effect. However, the 20Fe/C20h catalyst has an isotherm type H_4, where the hysteresis is more pronounced at low P/P_0 in water uptake.

The availability of Fe enhances the hydrophilicity both in unoxidized pristine and oxidized carbon, where a higher

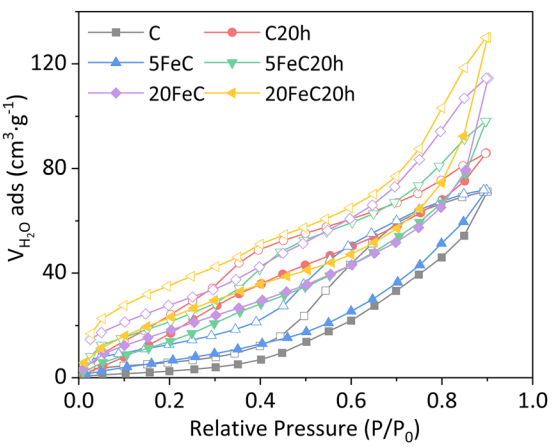

Fig. 2 Water vapor sorption isotherms of carbon supports and fresh catalysts.

loading of Fe results in higher water adsorption at low relative humidity. This is related to the high hydration energy of Fe^{3+} ion, which is reported to be −4430 kJ mol^{-1}.[45] The highest water uptake is obtained from the carbon with acid treatment and the highest Fe loading (20Fe/C20h catalyst). This is directly followed by the unoxidized 20Fe/C sample. In general, the improved hydrophilicity of the Fe-containing samples is likely caused by both the presence of iron oxide and by the reoxidation of the carbon surface occurring as a result of the decomposition of the iron precursor salt. These differences in hydrophilicity are becoming even more pronounced when considering that both samples have the lowest specific surface areas among all samples.

Measuring the contact angle of H_2O on a surface is a common technique to determine the wettability of catalysts.[39] Fig. 3 shows the contact angles of various carbon supports and catalysts using the sessile drop method. Using this method, hydrophobicity and hydrophilicity refer to contact angles higher and lower than 90°, respectively. The pristine carbon presented in Fig. 3(a) shows a high degree of hydrophobicity. After HNO_3 treatment for 20 h, the hydrophobic carbon becomes hydrophilic as the contact angle decreased from 152 to 60°, as shown in Fig. 3(b). A highly hydrophilic surface (30°) was obtained with 40 h of acid reflux treatment (Fig. S2a). The catalyst with 5 wt% Fe loading on the pristine carbon (5Fe/C, Fig. 3(c)) is less hydrophobic compared to the pristine hydrophobic carbon support, suggesting that the Fe-based nanoparticles have an affinity to H_2O and indicating reoxidation of the carbon surface during calcination. Bulk Fe_2O_3 typically demonstrates good wettability with a contact angle ranging from 10° to 40°.[46,47] The catalyst with 5 wt% Fe loading on the hydrophilic carbon support (5Fe/C20h, Fig. 3(d)) appears to show similar hydrophilicity compared to its carbon support (C20h, Fig. 3(b)). The same observation is made for 5Fe/C40h and C40h (Fig. S2b). In the case of 20Fe/C (Fig. 3(e)), the increased Fe loading for 20Fe/C results in a highly hydrophilic surface in comparison with C and 5Fe/C. 20Fe/C20h (Fig. 3(f)) shows the highest hydrophilicity among all catalysts due to the hydrophilic carbon support and higher Fe loading. 5Fe/C-700 (Fig. 3(g)), the catalyst with 5 wt% Fe loading pyrolyzed at 700 °C on the hydrophobic carbon, has similar wettability as 5Fe/C, indicating that the pyrolysis temperature has less influence on the catalysts based on the pristine carbon support. In addition, 5Fe/C20h-700 also shows rather hydrophobic properties (Fig. 3(h)).

In summary, the results from water vapour sorption and contact angle measurements are pointing to the fact that the oxidative pretreatment but also the decomposition of the iron precursor salt as well as the presence if the Fe-based nanoparticles are factors contributing to the increased hydrophilicity of the catalyst surface. In contrast, higher pyrolysis temperatures are leading to decreased hydrophilicity. This relationship can be well analyzed by looking the relationship between water vapor adsorption at $P/P_0 = 0.3$ and contact angle. At low relative pressure ($P/P_0 < 0.4$), adsorption of water molecules is dictated by the presence of surface functional groups rather than by the pore structures of the carbons.[48–51] The latter are anyways rather similar. In accordance, an inverse linear correlation between the water contact angle and the water sorption properties is found as displayed in Fig. 4.

Fig. 5 shows the TEM images of carbon supports and fresh catalysts. No significant difference could be observed between pristine hydrophobic carbon (C) and more hydrophilic HNO_3-treated carbon (C20h), as shown in Fig. 5(a) and (b), respectively. Fe nanoparticles of all catalysts are well-dispersed on the

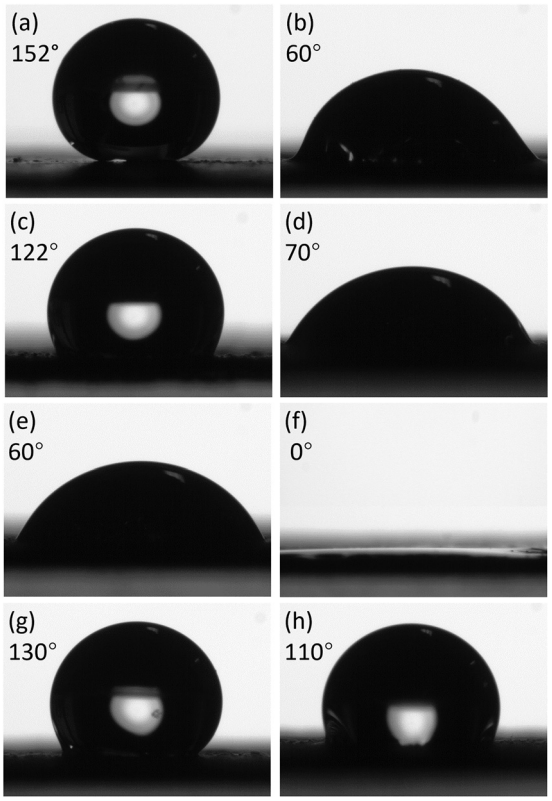

Fig. 3 Contact angles of carbon supports and fresh catalysts (a) C, (b) C20h, (c) 5Fe/C, (d) 5Fe/C20h, (e) 20Fe/C, (f) 20Fe/C20h, (g) 5Fe/C-700, and (h) 5Fe/C20h-700.

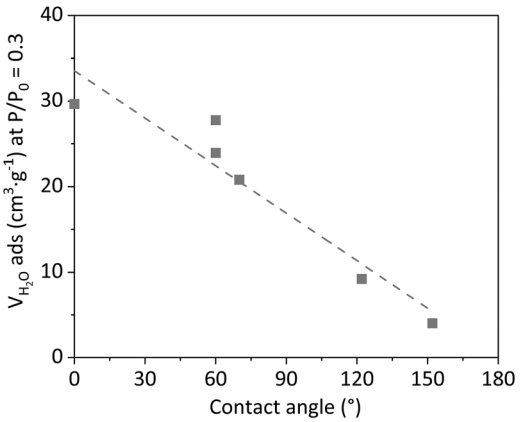

Fig. 4 The relationship between water vapor adsorption at $P/P_0 = 0.3$ and contact angle.

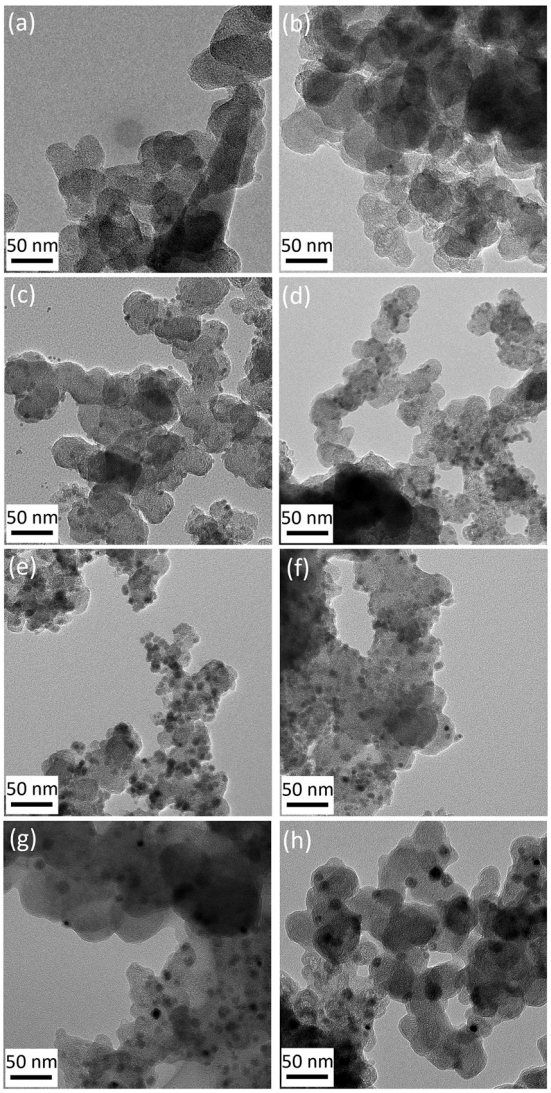

Fig. 5 TEM images of carbon supports and fresh catalysts (a) C, (b) C20h, (c) 5Fe/C, (d) 5Fe/C20h, (e) 20Fe/C, (f) 20Fe/C20h, (g) 5Fe/C-700, and (h) 5Fe/C20h-700.

carbon supports with the incipient wetness method.[52] The average particle sizes of fresh Fe nanoparticles are listed in Table 2, and the particle size distributions are shown in Fig. S3. Higher Fe loading and pyrolysis temperature result in larger nanoparticles. As for catalysts such as 5Fe/C20h, 5Fe/C40h, 20Fe/C20h and 5Fe/C20h-700, which utilize rather hydrophilic carbon supports, the average particle sizes and particle size distributions are similar to those of their counterparts with pristine hydrophobic carbons (5Fe/C, 20Fe/C, and 5Fe/C-700, respectively). This confirms that the hydrophilic carbon supports do not significantly affect fresh Fe nanoparticle size, thereby ruling out particle size effects in interpreting the catalytic performance. As can be expected from that, the catalysts with the same Fe loading and pyrolysis temperature after catalyst evaluation are comparable in activity since they attain similar CO_2 conversion under the same GHSV. The TEM images of spent catalysts and the particle size distributions are shown in Fig. S4 and S5, respectively. From Table 2, it can be seen that the average particle sizes of fresh and spent 5Fe/C and 5Fe/C-700 increase by approximately 50% due to particle sintering during activation and reaction. However, the average particle sizes of fresh and spent 5Fe/C20h, 5Fe/C40h, and 5Fe/C20h-700 remain similar, within the standard deviation range, indicating limited growth in nanoparticle size during activation and reaction. The presence of functional groups on the hydrophilic carbon support provides anchoring sites, thereby stabilizing the Fe nanoparticles.[53–55] Similar size increases of more than 100% over 20Fe/C and 20Fe/C/20h are observed, indicating that the functional groups on the hydrophilic carbon support no longer provide an effective anchoring effect. This behavior could be attributed to the higher Fe loading, which results in a closer interparticle distance between Fe nanoparticles. As reported by Yin *et al.*, when interparticle distances fall below a critical threshold, particle migration and coalescence are strongly enhanced, and this threshold depends sensitively on the strength of metal-support interactions.[56] Therefore, the short interparticle distances override the stabilizing effect of the carbon support in 20 wt% Fe loading catalysts.

Table 2 The Fe nanoparticle size of fresh and spent catalysts

Catalysts	$d_F \pm \sigma_F$[a] (nm)	$d_S \pm \sigma_S$[a] (nm)	TOS (h)
5Fe/C	6 ± 2	9 ± 4	25
5Fe/C20h	5 ± 1	5 ± 1	25
5Fe/C40h	5 ± 1	5 ± 1	25
20Fe/C	9 ± 2	21 ± 5	35
20Fe/C20h	8 ± 2	19 ± 5	35
5Fe/C-700	9 ± 2	14 ± 4	39
5Fe/C20h-700	11 ± 3	13 ± 4	39

[a] Measured by TEM.

3.2 Effect of hydrophilic and hydrophobic carbon supports on RWGS

To investigate the influence of more hydrophilic and more hydrophobic carbon supports on the RWGS reaction, the catalytic performance was investigated at 300 °C, 11 bar, $H_2/CO_2/Ar = 3/1/1$, and the corresponding data are presented in Table S1. Fig. 6(a) presents the CO_2 conversion as a function of residence time over 5Fe/C, 5Fe/C20h, and 5Fe/C40h catalysts. A positive relation between CO_2 conversion and residence time is observed for all catalysts. At a shorter residence time, there is no significant difference in CO_2 conversion between the catalysts. This may be attributed to the low residence times and CO_2 conversions below 10%, which likely result in insufficient H_2O partial pressure within the catalyst bed to exert a significant effect. However, with increasing residence times, 5Fe/C20h and 5Fe/C40h show a 3% lower CO_2 conversion compared to 5Fe/C. The rate of converted CO_2 and formed product per gram of Fe per second is expressed by iron time yield (FTY). Fig. 6(b) and (c) illustrate the relationship between the FTY of the formed product and the FTY of converted CO_2. As shown in Fig. 6(b), CO production rates increase linearly with CO_2 conversion rates for all catalysts. Fig. 6(c) shows that the hydrocarbon production rates appear to be independent of CO_2 conversion rates. Notably, the CO production rates are 5 to 20

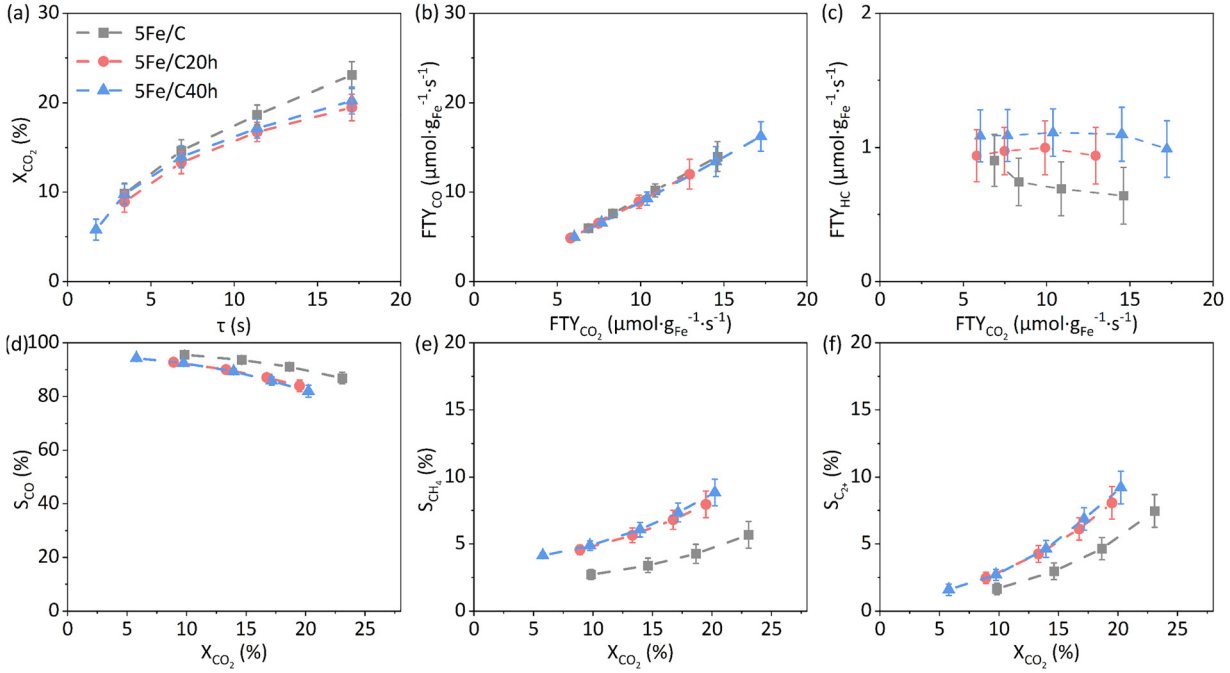

Fig. 6 Catalytic performance of 5Fe/C, 5Fe/C20h, and 5Fe/C40h: (a) CO_2 conversion as a function of residence time; (b) FTY of produced CO and (c) FTY of produced hydrocarbon as a function of FTY of CO_2; (d) CO selectivity, (e) CH_4 selectivity and (f) C_{2+} selectivity as a function of CO_2 conversion (300 °C, 11 bar, $H_2/CO_2/Ar$ = 3/1/1, 600–3000 mL g_{cat}^{-1} h^{-1}).

times higher than the hydrocarbon production rates for these catalysts. The CO production rates of all catalysts are comparable, but the hydrocarbon production rate of 5Fe/C is lower than those of 5Fe/C20h and 5Fe/C40h, suggesting that the more hydrophobic carbon support decreases FTS activity. The catalytic activities of 5Fe/C20h and 5Fe/C40h are relatively within experimental error, suggesting that the increased hydrophilicity has no significant effect.

To study the reaction pathways, product selectivities as a function of CO_2 conversion are plotted. As shown in Fig. 6(d), CO selectivity decreases slightly with increasing CO_2 conversions, indicating that RWGS is the primary reaction. The CO selectivity varies from 80% to 100% at 5% to 23% CO_2 conversion. The CO selectivity of 5Fe/C20h and 5Fe/C40h are lower than that of 5Fe/C, with a 3% decrease at 10% CO_2 conversion, and a 5% decrease at 20% CO_2 conversion. In contrast to CO selectivity, the CH_4 selectivity increases with increasing CO_2 conversion (Fig. 6(e)), and a non-zero CH_4 selectivity is observed when CO_2 conversion is extrapolated to zero. These indicate that the Sabatier reaction occurs as a primary reaction and is more prominent over the hydrophilic carbon-supported Fe-based catalysts. This could be attributed to the enhanced hydrogen transport from the hydrophilic carbon with the surface oxygen functional groups and defects.[57] From Fig. 6(f), it can be seen that C_{2+} hydrocarbons selectivity also increases with increasing CO_2 conversion, and a zero C_{2+} hydrocarbons selectivity is observed when CO_2 conversion is extrapolated to zero. Hence, FTS is clearly a secondary reaction. In line with the higher selectivity towards C_{2+} hydrocarbons, 5Fe/C20h and 5Fe/C40h show larger chain growth probabilities (Fig. S6). Interestingly, the selectivity-conversion plots for 5Fe/C20h and 5Fe/C40h completely overlap. This suggests that while the hydrophilic carbon supports influence catalytic performance, the number of functional groups does not seem to matter. A comparison of the RWGS catalysts reported in this work and those from the literature is provided in Table S2. Notably, the high CO selectivity achieved at CO_2 conversions approaching thermodynamic equilibrium highlights the suitability of our RWGS catalysts for integration with subsequent FTS.

The effect of hydrophilic and hydrophobic carbon supports on RWGS for 20Fe/C and 20Fe/C20h was also evaluated, as shown in Fig. 7. The comparable catalytic performance of the two catalysts indicates that the influence of support hydrophilicity is minimal. This is likely due to their overall hydrophilic character, as both 20Fe/C and 20Fe/C20h are intrinsically hydrophilic. Regarding the reaction pathway, CO selectivity decreases with the increasing selectivity toward CH_4 and C_{2+} hydrocarbons as CO_2 conversion increases. Notably, CO selectivity approaches 100% while hydrocarbon selectivity approaches zero when extrapolated to zero CO_2 conversion. This implies that RWGS is the only primary reaction, whereas FTS is just a secondary reaction, and no primary Sabatier reaction occurs over the 20Fe/C and 20Fe/C20h catalysts. Although their hydrophilic nature, in principle, could facilitate hydrogen transfer and promote the Sabatier reaction, this effect is counterbalanced by the suppression of transfer due to the higher Fe loading and larger Fe nanoparticle sizes.[57,58]

Based on the above discussion, for the 5 wt% Fe loading catalysts, hydrogen transport from the surface of the carbon support to the Fe nanoparticles is significant, thus the

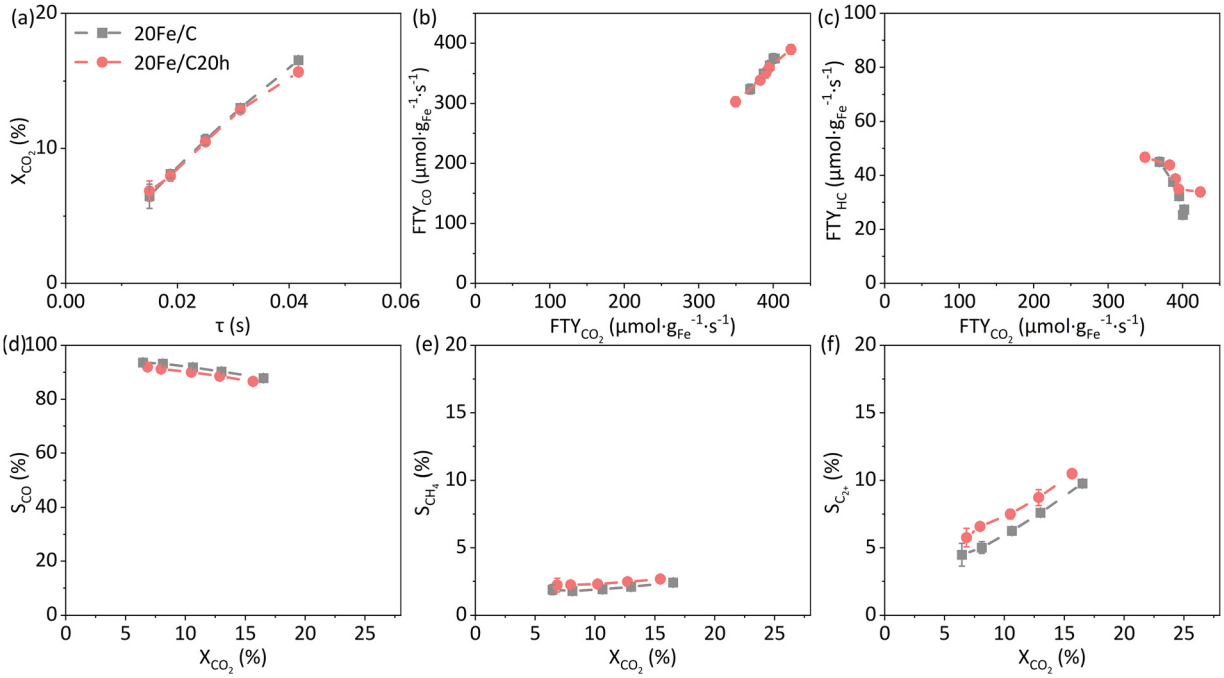

Fig. 7 Catalytic performance of 20Fe/C and 20Fe/C20h: (a) CO_2 conversion as a function of residence time; (b) FTY of produced CO and (f) FTY of produced hydrocarbon as a function of FTY of CO_2; (d) CO selectivity, (e) CH_4 selectivity and (f) C_{2+} selectivity as a function of CO_2 conversion (300 °C, 11 bar, $H_2/CO_2/Ar$ = 3/1/1, 180 000–500 000 mL g_{cat}^{-1} h^{-1}).

hydrophilic/hydrophobic nature of the support can strongly influence the reaction pathway. In this case, hydrophilic supports enhance hydrogen transfer, which promotes the Sabatier reaction as a primary reaction and reduces CO selectivity while increasing CH_4 and C_{2+} selectivities. Recent studies have demonstrated that a hydrophilic surface with a hydroxyl group exhibited a higher chain growth probability due to water or hydroxyl-assisted activation.[59–62] In the water-assisted pathway, H_2O or H_2O derivatives can reduce the energy barrier of H-assisted C–O dissociation and activate the formation of intermediates by facilitating H transfer.[63] This leads to an increased concentration of CH* monomers and boosts chain growth. In contrast, for the 20 wt% Fe loading catalysts, the dominant hydrogen source is adsorption directly on the Fe particles. The larger Fe nanoparticle size and higher Fe loading suppress hydrogen transfer, thereby reducing the influence of support hydrophobicity and explaining the negligible differences observed between hydrophilic and hydrophobic supports. As a result, the effect of the water-assisted pathway is much less pronounced for the 20 wt% Fe loading catalysts, and almost no primary Sabatier reaction occurs. Instead, the RWGS dominates as the primary reaction.

3.3 Effect of hydrophilic and hydrophobic carbon supports on FTS

Since the FTS reaction is a secondary reaction, a higher CO_2 conversion is necessary to evaluate the effect of the hydrophilic carbon support on FTS performance. Typically, higher CO_2 conversion could be achieved with lower GHSV or/and higher temperatures. However, due to limitations in our reactor configuration that precluded operation at lower GHSV, increased CO_2 conversion was instead achieved by increasing Fe loading and Fe nanoparticle sizes.[52] Fig. 8 presents the catalytic performances of 20Fe/C and 20Fe/C20h, and the results are largely comparable. As shown in Fig. 8(a), the CO_2 conversion for the two catalysts differs by less than 1% at identical residence time. A positive correlation can be found between the CO production rate and CO_2 conversion rate (Fig. 8(b)). At a lower CO_2 conversion rate, a minor difference is observed between 20Fe/C and 20Fe/C20h. As the CO_2 conversion rate increases, 20Fe/C shows a higher CO production rate, and the divergence becomes more pronounced. This is attributed to the effect of GHSV. With respect to the hydrocarbon production rate, the increase is higher when the CO_2 conversion rate is <100 μmol g_{Fe}^{-1} s^{-1}. When the CO_2 conversion rate is $>$ 100 μmol g_{Fe}^{-1} s^{-1}, the growth rate slows for 20Fe/C20h while it levels off and remains stable for 20Fe/C (Fig. 8(c)). This suggests that the hydrocarbon production rate is limited by the CO_2 conversion rate (>100 μmol g_{Fe}^{-1} s^{-1}). Notably, 20Fe/C20h achieves a higher hydrocarbon production rate compared to 20Fe/C, implying a faster FTS reaction over the catalyst on the more hydrophilic carbon support. Meanwhile, 20Fe/C20h exhibits higher CH_4 and C_{2+} production rates (Fig. S7).

As shown in Fig. 8(d)–(f), CO selectivity decreases corresponding to an increase in hydrocarbon formation as CO_2 conversion rises, while no hydrocarbon can be obtained at zero CO_2 conversion, indicating that FTS occurs exclusively as a secondary reaction. Besides, 20Fe/C20h shows a slightly lower CO selectivity ($<4\%$) and a slightly higher CH_4 and C_{2+}

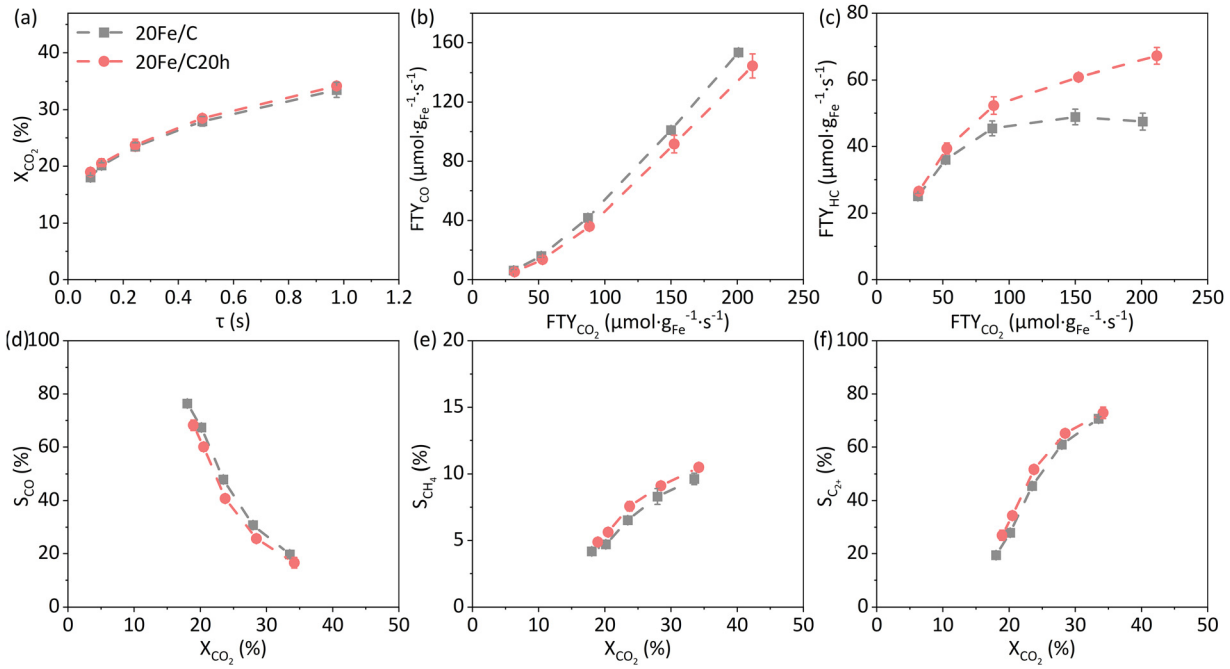

Fig. 8 Catalytic performance of 20Fe/C and 20Fe/C20h: (a) CO_2 conversion as a function of residence time; (b) FTY of produced CO and (f) FTY of produced hydrocarbon as a function of FTY of CO_2; (d) CO selectivity, (e) CH_4 selectivity and (f) C_{2+} selectivity as a function of CO_2 conversion (300 °C, 11 bar, $H_2/CO_2/Ar$ = 3/1/1, 7500–90 000 mL g_{cat}^{-1} h^{-1}).

selectivity (<1% and <3%, respectively) in comparison to 20Fe/C. Nevertheless, they have similar hydrocarbon distribution and chain growth probability (Fig. S8). These results indicate that the carbon support hydrophilicity has a limited effect on catalytic performance.

As both 20Fe/C and 20Fe/C20h catalysts are rather hydrophilic, a different preparation approach to attain larger Fe nanoparticles with overall hydrophobicity was investigated. Specifically, the 5 wt% Fe catalysts on C and C20h supports were pyrolyzed at 700 °C. The catalytic performance of 5Fe/C-700 and 5Fe/C20h-700 catalysts is summarized in Fig. S9. The curves of CO_2 conversion *versus* residence time and the CO and hydrocarbon production rate *versus* CO_2 conversion rate almost overlap (Fig. S9(a)–(c)). Regarding the product selectivity, 5Fe/C20h-700 displays lower CO selectivity compared to 5Fe/C-700, which correlates with higher C_{2+} selectivity, as illustrated in Fig. S9(d) and (f). These findings suggest that neither H_2O partial pressure nor the hydrophobicity of the catalysts are key factors influencing the structure–performance relationship for FTS in this study.

3.4 Fe phases evolution

Mössbauer spectroscopy was used to explore the evolution of Fe phases, and corresponding spectra are shown in Fig. S10. Detailed fitting parameters are provided in Tables S3 and S4. The data for 5Fe/C and 20Fe/C were obtained from our previous study.[52] Fresh catalysts were measured at 4.2 K, as the Fe structures were superparamagnetic at 120 K. All fresh catalysts consist exclusively of Fe_2O_3, as shown in Fig. S11. All other spectra were recorded at 120 K, which is low enough to mitigate potential issues arising from Debye temperature differences among different Fe sites. The Fe phase distributions are

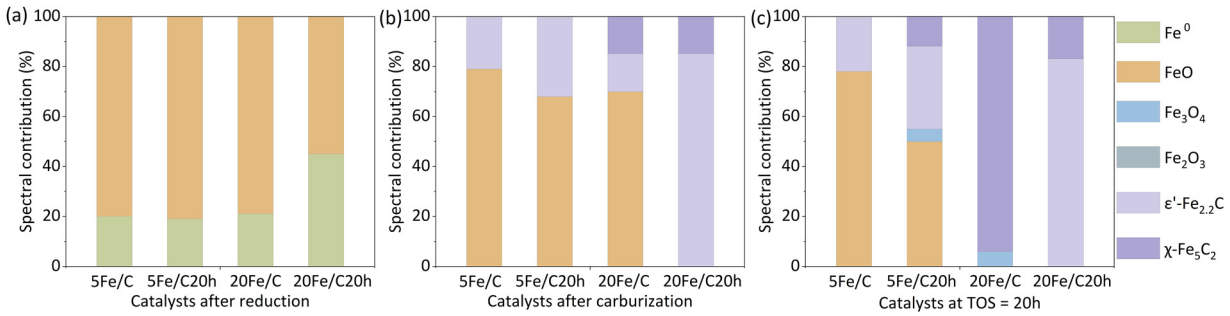

Fig. 9 Distribution of Fe phases in 5Fe/C, 5Fe/C20h, 20Fe/C, and 20Fe/C20h (a) after reduction, (b) after carburization, and (c) at TOS = 20 h from Mössbauer spectra.

summarized in Fig. 9. For the RWGS catalysts after reduction, both 5Fe/C and 5Fe/C20h contain 20% metallic Fe and 80% FeO, indicating that the more hydrophilic carbon support has no significant influence on reducibility. In contrast, for the FTS catalysts, 20Fe/C contains 21% metallic Fe, while 20Fe/C20h has 45% metallic Fe, suggesting that the more hydrophilic carbon support promotes the reduction, possibly due to enhanced Fe dispersion, especially with a higher Fe loading. After carburization, for the RGWS catalysts, 5Fe/C consists of 21% ε′-$Fe_{2.2}C$ and 79% FeO, whereas 5Fe/C20h contains 32% ε′-$Fe_{2.2}C$ and 68% FeO, indicating that the more hydrophilic support facilitates carburization. For the FTS catalysts, 20Fe/C comprises 15% ε′-$Fe_{2.2}C$, 15% χ-Fe_5C_2, and 70% FeO, whereas 20Fe/C20h shows 26% ε′-$Fe_{2.2}C$ and 74% χ-Fe_5C_2, further supporting the conclusion that the more hydrophilic carbon support enhances carburization. For the RWGS catalysts under reaction conditions, 5Fe/C still primarily contains FeO (79%), which is likely responsible for RWGS activity. In contrast, 5Fe/C20h contains 33% ε′-$Fe_{2.2}C$, 12% χ-Fe_5C_2, 5% Fe_3O_4, and 50% FeO. The lower content of Fe oxide is associated with a decrease in CO selectivity. Moreover, the higher degree of carburization correlates with increased C_{2+} selectivity, longer chain growth probability, and higher hydrocarbon production rate. For the FTS catalysts, 20Fe/C is almost fully carburized, containing 94% χ-Fe_5C_2 and 6% Fe_3O_4, while 20Fe/C20h is deeply carburized, consisting of 83% ε′-$Fe_{2.2}C$ and 17% χ-Fe_5C_2. The existence of Fe_3O_4 in 20Fe/C may account for its relatively higher CO selectivity *via* the RWGS reaction. The fully developed Fe carbide phases in 20Fe/C20h likely contribute to its significantly enhanced hydrocarbon production rate. The slight difference in the content of Fe carbide may be responsible for the subtle variations in their catalytic performance.

4. Conclusion

In this study, the effects of more hydrophobic and more hydrophilic carbon-supported Fe-based catalysts on the RWGS and FTS reactions were investigated. The oxidation of carbon supports through HNO_3 treatment effectively modified its surface properties, transforming hydrophobicity into hydrophilicity. However, the overall hydrophilicity of the catalysts is found to depend on both the carbon support and the Fe loading, as Fe nanoparticles also exhibit hydrophilic characteristics. The relative H_2O affinity of the catalysts determined by H_2O vapor sorption measurements and contact angle measurements is consistent. Catalytic performance was performed at 300 °C, 11 bar, $H_2/CO_2/Ar$ = 3/1/1, 600–500 000 mL g_{cat}^{-1} h^{-1}. RWGS is investigated at CO_2 conversions below the thermodynamic equilibrium limit of 23% using the 5 wt% Fe and 20 wt% Fe loading catalysts. For the 5 wt% Fe loading catalysts, the more hydrophobic catalysts exhibit higher activity and CO selectivity compared to the hydrophilic catalysts. Notably, the Sabatier reaction emerges as a competing pathway, particularly over the more hydrophilic carbon-supported Fe-based catalysts. This enhanced CO_2 methanation is likely due to the hydrogen transfer from the carbon support, which is promoted by the surface oxygen functional groups and defects over the more hydrophilic carbon. Hydrogen transfer from the carbon support to the Fe nanoparticles is significant for the 5 wt% Fe catalysts, thus the hydrophilic/hydrophobic nature of the support influences the reaction pathway. Mössbauer spectroscopy reveals that the catalyst supported on more hydrophilic carbon contains less Fe oxide and a higher degree of carburization than those on hydrophobic carbon, correlating with their enhanced hydrocarbon productivity. On the other hand, for the 20 wt% Fe loading catalysts, the support hydrophilicity has negligible influence on both RWGS and FTS, due to their overall hydrophilic character from the high Fe loading. Furthermore, Mössbauer spectroscopy confirms that these two catalysts contain comparable amounts of Fe carbide. Hydrogen activation occurs mainly *via* direct adsorption on Fe nanoparticles, and the larger particle size and higher Fe loading suppress hydrogen transfer, minimizing the role of support hydrophilicity. Consequently, RWGS dominates as the primary reaction, with almost no Sabatier reaction observed.

Author contributions

Weixin Meng: writing – review & editing, writing – original draft, validation, methodology, investigation, formal analysis, data curation, conceptualization. Sri Rezeki: writing – review & editing, validation, resources, methodology, investigation, formal analysis, data curation, conceptualization. A. Iulian Dugulan: writing – review & editing, validation, resources, methodology, investigation, formal analysis, data curation, conceptualization. Martin Oschatz: writing – review & editing, validation, resources, methodology, investigation, formal analysis, data curation, conceptualization. Jingxiu Xie: writing – review & editing, writing – original draft, supervision, resources, project administration, methodology, funding acquisition, formal analysis, conceptualization.

Conflicts of interest

There are no conflicts to declare.

Data availability

The data that support the findings of this study are available from the corresponding author upon reasonable request.

Supplementary information is available. See DOI: **https://doi.org/10.1039/d5ma00785b**.

Acknowledgements

Weixin Meng acknowledges financial support from the China Scholarship Council (CSC): no. 202106460008.

References

1 C. Kim, C. Yoo, H. Oh, B. K. Min and U. Lee, *J. CO_2* Util., 2022, **65**, 102239.

2 A. Saravanan, P. S. Kumar, D. N. Vo, S. Jeevanantham, V. Bhuvaneswari, V. A. Narayanan, P. R. Yaashikaa, S. Swetha and B. Reshma, *Chem. Eng. Sci.*, 2021, **236**, 116515.
3 S. Saeidi, S. Najari, V. Hessel, K. Wilson, F. J. Keil, P. Concepción, S. L. Suib and A. E. Rodrigues, *Prog. Energy Combust. Sci.*, 2021, **85**, 100905.
4 J. Hu, Y. Wang, X. Zhang, Y. Wang, G. Yang, L. Shi and Y. Sun, *Int. J. Hydrogen Energy*, 2024, **59**, 1023–1041.
5 B. Dai, G. Zhou, S. Ge, H. Xie, Z. Jiao, G. Zhang and K. Xiong, *Can. J. Civ. Eng.*, 2017, **95**, 634–642.
6 Z. Gou, C. Huang, G. Zhou, X. Ren, L. Deng, T. Wang and Q. Peng, *J. CO_2* Util., 2024, **81**, 102728.
7 X. Zhao, Z. Wu, J. Fu, J. Guo and S. Kang, *ACS Appl. Mater. Interfaces*, 2021, **13**, 57100–57106.
8 J. E. Apolinar-Hernández, S. L. Bertoli, H. G. Riella, C. Soares and N. Padoin, *Energy Fuels*, 2024, **38**(1), 1–28.
9 T. P. Minyukova and E. V. Dokuchits, *Int. J. Hydrogen Energy*, 2023, **48**(59), 22462–22483.
10 J. Liu, Y. Zhang and C. Peng, *ACS Omega*, 2024, **9**(24), 25610–25624.
11 L. Krausser, Q. Yang and E. V. Kondratenko, *ChemCatChem*, 2024, **16**, e202301716.
12 S. Lyu, L. Wang, Z. Li, S. Yin, J. Chen, Y. Zhang, J. Li and Y. Wang, *Nat. Commun.*, 2020, **11**, 6219.
13 L. Brübach, D. Hodonj and P. Pfeifer, *Ind. Eng. Chem. Res.*, 2022, **61**, 1644–1654.
14 L. Jiang, K. Li, W. N. Porter, H. Wang, G. Li and J. G. Chen, *J. Am. Chem. Soc.*, 2024, **146**, 2857–2875.
15 S. Zhang, K. Wang, F. He, X. Gao, S. Fan, Q. Ma, T. Zhao and J. Zhang, *Molecules*, 2023, **28**(14), 5521.
16 L. Lin, Y. Ge, H. Zhang, M. Wang, D. Xiao and D. Ma, *JACS Au*, 2021, **1**(11), 1834–1848.
17 Z. Yan, P. Shi, J. Wang, Y. Song, H. Ban and C. Li, *ChemCatChem*, 2024, **16**, e202401135.
18 V. R. R. Pendyala, G. Jacobs, J. C. Mohandas, M. Luo, H. H. Hamdeh, Y. Ji, M. C. Ribeiro and B. H. Davis, *Catal. Lett.*, 2010, **140**, 98–105.
19 J. Zhu, P. Wang, X. Zhang, G. Zhang, R. Li, W. Li, T. P. Senftle, W. Liu, J. Wang, Y. Wang, A. Zhang, Q. Fu, C. Song and X. Guo, *Sci. Adv.*, 2022, **8**, eabm3629.
20 M. Claeys, E. Steen, T. Botha, R. Crous, A. Ferreira, A. Harilal, D. J. Moodley, P. Moodley, E. Plessis and J. L. Visagie, *ACS Catal.*, 2021, **11**(22), 13866–13879.
21 Y. Xu, H. Liang, R. Li, Z. Zhang, C. Qin, D. Xu, H. Fan, B. Hou, J. Wang, X. Gu and M. Ding, *Angew. Chem., Int. Ed.*, 2023, **62**, e202306786.
22 S. Li, X. Liu, Y. Lu, T. Lin, K. Gong, C. Wang, Y. An, F. Yu, L. Zhong and Y. Sun, *Appl. Catal., A*, 2022, **635**, 118552.
23 Y. Xu, X. Li, J. Gao, J. Wang, G. Ma, X. Wen, Y. Yang, Y. Li and M. Ding, *Science*, 2021, **371**, 610–613.
24 Z. Zhang, B. Chen, L. Jia, W. Liu, X. Gao, J. Gao, B. Meng, Y. Tan, Y. He, W. Tu and Y. Han, *Appl. Catal., B*, 2023, **327**, 122449.
25 C. G. Okoye-Chine, M. Moyo and D. Hildebrandt, *J. Ind. Eng. Chem.*, 2021, **97**, 426–433.
26 F. Ding, A. Zhang, M. Liu, X. Guo and C. Song, *RSC Adv.*, 2014, **4**, 8930–8938.
27 E. Rytter, A. R. Salman, N. E. Tsakoumis, R. Myrstad, J. Yang, S. Lögdberg, A. Holmen and M. Rønning, *Catal. Today*, 2018, **299**, 20–27.
28 C. G. Okoye-Chine, M. Moyo and D. Hildebrandt, *Fuel*, 2021, **296**, 120667.
29 C. G. Okoye-Chine, M. Moyo and D. Hildebrandt, *Rev. Chem. Eng.*, 2022, **38**(5), 477–502.
30 I. C. Gerber and P. Serp, *Chem. Rev.*, 2020, **120**(2), 1250–1349.
31 K. Chen, Y. Li, M. Wang, Y. Wang, K. Cheng, Q. Zhang, J. Kang and Y. Wang, *Small*, 2021, **17**, 2007527.
32 M. D. Sánchez, P. Chen, T. Reinecke, M. Muhler and W. Xia, *ChemCatChem*, 2012, **4**, 1997–2004.
33 G. Wang, L. Chen, Y. Sun, J. Wu, M. Fu and D. Ye, *RSC Adv.*, 2015, **5**, 45320–45330.
34 N. L. Visser, J. C. Verschoor, L. C. J. Smulders, F. Mattarozzi, D. J. Morgan, J. D. Meeldijk, J. E. S. van der Hoeven, J. A. Stewart, B. D. Vandegehuchte and P. E. de Jongh, *Catal. Today*, 2023, **418**, 114071.
35 L. M. Chew, P. Kangvansura, H. Ruland, H. J. Schulte, C. Somsen, W. Xia, G. Eggeler, A. Worayingyong and M. Muhler, *Appl. Catal., A*, 2014, **482**, 163–170.
36 S. M. G. Lama, J. L. Weber, T. Heil, J. P. Hofmann, R. Yan, K. P. de Jong and M. Oschatz, *Appl. Catal., A*, 2018, **568**, 213–220.
37 M. Oschatz, J. P. Hofmann, T. W. van Deelen, W. S. Lamme, N. A. Krans, E. J. M. Hensen and K. P. de Jong, *ChemCatChem*, 2017, **9**, 620–628.
38 W. Xia, *Catal. Sci. Technol.*, 2016, **6**, 630–644.
39 E. Nowak, G. Combes, E. H. Stitt and A. W. Pacek, *Powder Technol.*, 2013, **233**, 52–64.
40 A. A. Abd, M. R. Othman and J. Kim, *Environ. Sci. Pollut. Res.*, 2021, **28**, 43329–43364.
41 P. Düngen, R. Schlogl and S. Heumann, *Carbon*, 2018, **130**, 614–622.
42 X. Gong, Z. Guo and Z. Wang, *Combust. Flame*, 2010, **157**, 351–356.
43 C. O. Ania, J. B. Parra and J. J. Pis, *Fuel Process. Technol.*, 2002, **79**, 265–271.
44 M. Thommes, K. Kaneko, A. V. Neimark, J. P. Olivier, F. Rodriguez-Reinoso, J. Rouquerol and K. S. W. Sing, *Pure Appl. Chem.*, 2015, **87**, 1051–1069.
45 M. Uudsemaa and T. Tamm, *Chem. Phys. Lett.*, 2004, **400**(1–3), 54–58.
46 Z. Landolsi, I. B. Assaker, D. Nunes, E. Fortunato, R. Martins, R. Chtourou and S. Ammar, *J. Mater. Sci.: Mater. Electron.*, 2020, **31**, 20753–20773.
47 J. I. Peña-Flores, E. Sánchez-Mora, J. J. Gervacio-Arciniega, M. Toledo-Solano and C. Márquez-Beltrán, *J. Adhes. Sci. Technol.*, 2021, **35**(4), 386–405.
48 L. Sarkisov, A. Centineo and S. Brandani, *Carbon*, 2017, **118**, 127e138.
49 W. H. Lee and P. J. Reucroft, *Carbon*, 1999, **37**, 7–14.
50 C. Atalay-Oral and M. Tatlier, *Adsorption*, 2024, **30**, 673–684.
51 E. P. Ng and S. Mintova, *Microporous Mesoporous Mater.*, 2008, **114**, 1–26.

52 W. Meng, B. C. A. de Jong, H. van de Bovenkamp, G. Boer, G. L. Bezemer, A. I. Dugulan and J. Xie, *Chem. Eng. J.*, 2024, **489**, 151166.
53 A. Karimi, B. Nasernejad, A. M. Rashidi, A. Tavasoli and M. Pourkhalil, *Fuel*, 2014, **117**, 1045–1051.
54 A. N. Pour, M. R. Housaindokht and S. M. K. Shahri, *Ind. Eng. Chem. Res.*, 2018, **57**, 13639–13649.
55 T. Fu, R. Liu, J. Lv and Z. Li, *Fuel Process. Technol.*, 2014, **122**, 49–57.
56 P. Yin, S. Hu, K. Qian, Z. Wei, L. Zhang, Y. Lin, W. Huang, H. Xiong, W. Li and H. Liang, *Nat. Commun.*, 2021, **12**, 4865.
57 H. Shen, H. Li, Z. Yang and C. Li, *Green Energy Environ.*, 2022, **7**, 1161e1198.
58 Y. Zhou, J. Wang, L. Liang, Q. Sai, J. Ni, C.-T. Au, X. Lin, X. Wang, Y. Zheng, L. Zheng and L. Jiang, *J. Catal.*, 2021, **404**, 501–511.
59 Y. Zhang, X. Guo, B. Liu, J. Zhang, X. Gao, Q. Ma, S. Fan and T. Zhao, *Fuel*, 2021, **294**, 120504.
60 Y. Zhang, X. Guo, B. Liu, J. Zhang, X. Gao, Q. Ma, S. Fan and T. Zhao, *Fuel*, 2021, **305**, 121473.
61 B. Liu, J. Liang, X. Gao, Q. Ma, J. Zhang and T. Zhao, *Fuel*, 2022, **326**, 125054.
62 C. Wang, X. Gao, J. Zhang, Q. Ma, S. Fan and T. Zhao, *Appl. Surf. Sci.*, 2024, **658**, 159820.
63 E. Rytter and A. Holmen, *Top. Catal.*, 2018, **61**, 1024–1034.